Constraints on Inner Core Anisotropy Using Array Observations of P'P'

Daniel A. Frost, Barbara Romanowicz

AGU PUBLICATIONS

Geophysical Research Letters

RESEARCH LETTER
10.1002/2017GL075049

Key Points:
- Detect inner core phase P′P′df (PKPP KPdf) at two high latitude seismic arrays
- Infer weak inner core anisotropy of 0.5–1.5% aligned with the rotation axis
- Observe stronger velocity anomalies with greater variability in magnitude in paths reflecting under the South Sandwich Islands

Supporting Information:
- Supporting Information S1
- Table S1

Correspondence to:
D. A. Frost,
dafrost@berkeley.edu

Citation:
Frost, D. A. & Romanowicz, B. (2017). Constraints on inner core anisotropy using array observations of P′P′. *Geophysical Research Letters*, *44*, 10,878–10,886. https://doi.org/10.1002/2017GL075049

Received 21 JUL 2017
Accepted 13 OCT 2017
Accepted article online 20 OCT 2017
Published online 4 NOV 2017

Constraints on Inner Core Anisotropy Using Array Observations of P′P′

Daniel A. Frost[1] and **Barbara Romanowicz**[1,2,3]

[1]Earth and Planetary Science, University of California, Berkeley, CA, USA, [2]Institut de Physique du Globe de Paris, Paris, France, [3]College de France, Paris, France

Abstract Recent studies of PKPdf travel times suggest strong anisotropy (4% or more) in the quasi-western inner core hemisphere. However, the availability of paths sampling at low angles to the Earth's rotation axis (the fast axis) is limited. To augment this sampling, we collected a travel time data set for the phase P′P′df (PKPPKPdf), for which at least one inner core leg is quasi-polar, at two high latitude seismic arrays. We find that the inferred anisotropy is weak (on the order of 0.5 to 1.5%), confirming previous results based on a much smaller P′P′ data set. While previous models of inner core anisotropy required very strong alignment of anisotropic iron grains, our results are more easily explained by current dynamic models of inner core growth. We observe large travel time anomalies when one leg of P′P′df is along the South Sandwich to Alaska path, consistent with PKPdf observations, and warranting further investigation.

1. Introduction

Inner core anisotropy with the fast axis aligned with the Earth's rotation axis was proposed 30 years ago based on observations of seismic body waves traveling faster along paths close to the Earth's rotation axis than those traveling equatorially (Morelli et al., 1986) and on anomalous splitting of core-sensitive normal modes (Woodhouse et al., 1986). Continued investigation has refined measurements of the velocity structure of the inner core, revealing increasing complexity (for review see Deuss, 2014; Tkalcic, 2015). In the most recent models, the inner core consists of two roughly equal hemispheres with different levels of *P*-velocity anisotropy: up to 4.8% in the quasi-western hemisphere and up to 1.4% in the quasi-eastern hemisphere (Irving & Deuss, 2011; Tanaka & Hamaguchi, 1997). The location and depth extent of the boundaries is not well constrained (Irving, 2016; Lythgoe et al., 2014). Depth dependence of the anisotropy has been proposed, along with evidence for a distinct innermost inner core of 300–600 km in radius, with anisotropy inclined to the rotation axis (Beghein & Trampert, 2003; Cao & Romanowicz, 2007; Ishii & Dziewonski, 2002; Sun & Song, 2008; Wang et al., 2015).

The seismically inferred anisotropy motivates studies of inner core mineral texture and composition. The proportion and nature of any light element in the inner core affects bulk properties (e.g., Nguyen & Holmes, 2004), while crystal structure and alignment impacts anisotropy (e.g., Wenk et al., 2000). The growth behavior of the inner core may have influenced the development of anisotropy (Lincot et al., 2015; Monnereau et al., 2010). Accurate understanding of the distribution of velocities in the inner core will inform its formation and deformation history.

Absolute PKPdf residual travel times with respect to 1D isotropic reference models are sensitive to errors in source parameters and to uncorrected mantle heterogeneity. To minimize these effects, they are often referred to a core phase that does not interact with the inner core, such as PKPab or PKPbc. Unfortunately, there are few PKPdf measurements for paths close to the rotation axis, due to the global distribution of earthquakes and stations. Furthermore, many of these paths correspond to sources in the South Sandwich Islands (SSI) observed in Alaska and Siberia. These particular paths show large variability in PKPdf travel time anomalies (Romanowicz et al., 2003; Romanowicz & Wenk, 2017; Tkalcic, 2010). While large residuals are observed on some polar paths (implying up to 8.8% velocity anisotropy, e.g., Lythgoe et al., 2014), owing to the limited sampling, these measurements may not be representative of the whole inner core. Further, independent travel time measurements of inner core sensitive phases are necessary to constrain the magnitude and spatial extent of anisotropy.

The phase P′P′df is the underside surface reflection of the PKPdf wave, and it traverses the inner core twice (Figure 1a). It allows different sampling of the inner core than is available in PKPdf studies (Figures 1b and 1c).

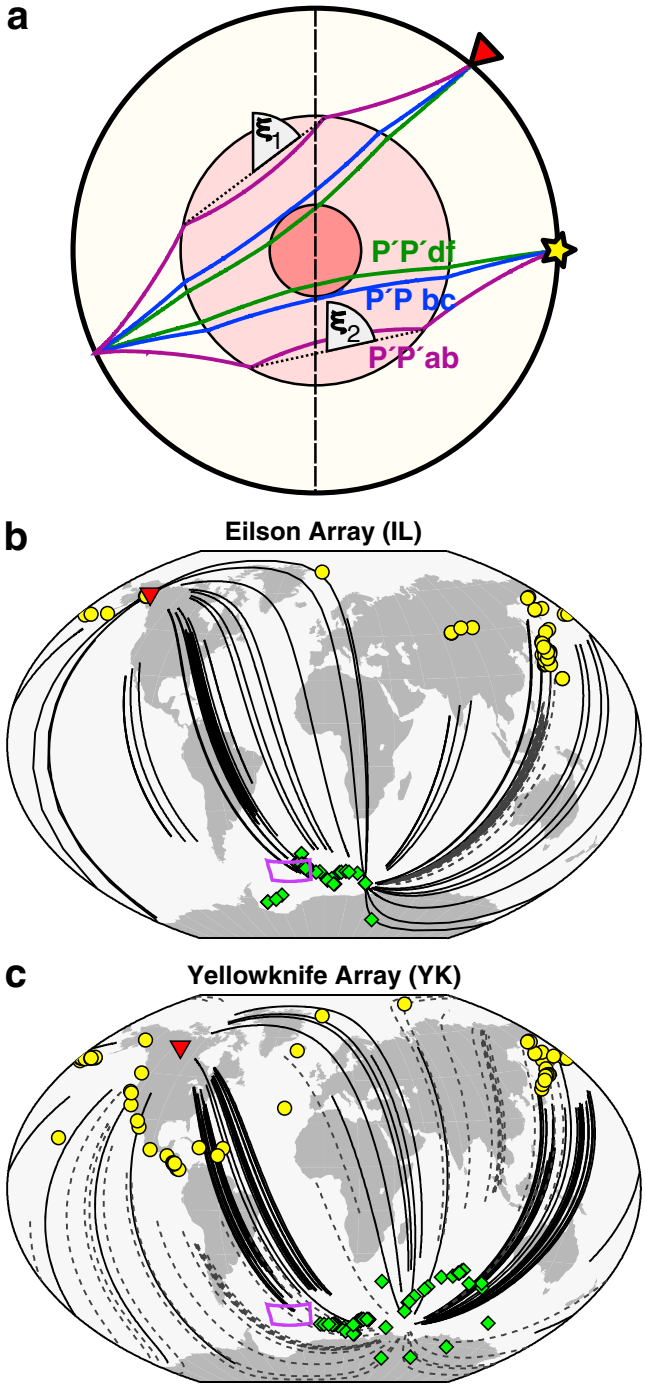

Figure 1. (a) Phases of P′P′ (also written PKPPKP). Angles of the inner core paths relative to the rotation axis (dashed line) are represented by ξ_1 and ξ_2 for source and receiver-side paths, respectively. Distribution of inner core paths between sources (circles), surface reflection points (diamonds), and arrays (triangles) for events to (b) Eilson and (c) Yellowknife arrays. Polar ($\xi \leq 35°$) and equatorial ($\xi > 35°$) paths are drawn as solid and dashed lines, respectively. The box describes the source region of South Sandwich Island earthquakes.

Following Bréger, Romanowicz, et al. (2000) and Rost and Garnero (2004), we measured P′P′df residual times along previously unsampled paths, spanning a range of angles (ξ) made by the path in the inner core with the rotation axis. Previous studies of the inner core using these phases did not find evidence of strong anisotropy.

2. Methods

We collected data from 256 $M > 6$ events that occurred within 0 to 65° epicentral distance of two high-latitude IMS arrays, Eilson (IL) in Alaska and Yellowknife (YK) in Canada from 1995 to 2012 (Table S1 in the supporting information). Origin times and event locations are taken from the Reviewed Event Bulletin (REB, International Seismological Centre, 2014). The two P′P′df legs pass through the inner core at different angles to the rotation axis. In our data set many paths have one inner core leg inclined within 35° of the rotation axis (often the receiver-side leg) and a second leg oriented equatorially (Figure S1 in the supporting information). Most paths in our data set (60%) turn in a limited depth range between 5,321 and 5,621 km. Deeper paths do not cover a sufficient range of ξ angles for us to resolve depth dependence of anisotropy.

P′P′df is a low amplitude phase, having twice traveled through the strongly attenuating inner core (e.g., Li & Cormier, 2002); thus, we stack traces to amplify the phase relative to the noise. We filter data between 0.4 and 1.5 Hz; select a time window around the predicted arrivals of P′P′df, P′P′bc, and P′P′ab; and beam traces on slownesses from 0 to 8 s/deg and back-azimuths from −180 to 180° (relative to the great circle path) (Davies et al., 1971). From the linear beams we calculate *F*-vespagrams by applying the *F*-statistic, a coherence measure that is effective at suppressing aliasing, thus sharpening the slowness and back-azimuth resolution at an array (equation (1); Blandford, 1974; Selby, 2008). The coherence, *F*, is computed from the ratio of the sum of the energy in the beam, *b*, to the summed differences between the beam and each trace used to form the beam, x_i, in a time window, *M*, normalized by the number of traces in the beam, *N*.

$$F = \frac{N-1}{N} \frac{\Sigma_{t=1}^{M} b(t)^2}{\Sigma_{t=1}^{M} \Sigma_{i=1}^{N} (x_i(t) - b(t))^2} \quad (1)$$

Using both slowness-time and backazimuth-time *F*-vespagrams, individual beams, and *F*-traces (Figure 2; see Figures S2–S6 for vespagrams of other qualities), we handpick the onsets of P′P′df, P′P′ab, and P′P′bc, where present, measured relative to predictions from model ak135 (Kennett et al., 1995), corrected for ellipticity (Kennett & Gudmundsson, 1996). We visually assess waveform similarities between phases to aid identification. The P′P′ab waveform is Hilbert transformed for comparison with the P′P′df waveform. Slowness and back-azimuth are used to aid picking of the specular reflections and to help with discounting contamination from other events or phases. We only select signals arriving within ~30° of the great circle path at slownesses within 1 s/deg of those predicted by ak135. We use a similar method of *F*-vespagrams and beams to measure the direct *P* wave travel time anomaly for each event relative to ak135, corrected for ellipticity.

Where present, phases are picked as poor or good, dependent on the above characteristics. We discard 141 events, leaving 115 well-picked events (57 at IL and 58 at YK), each with at least a P′P′df phase, and possibly a

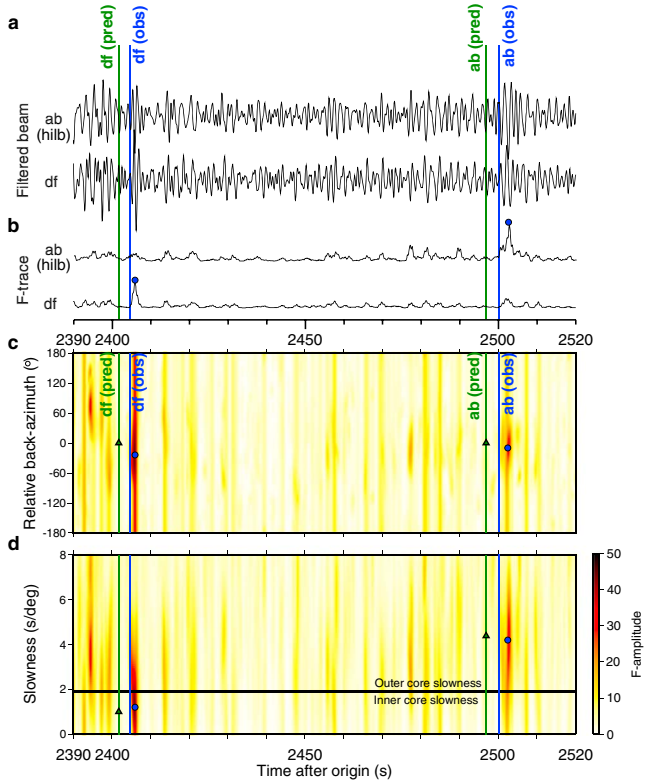

Figure 2. Beams and array processing of a *M*6.5 event that occurred on 15 August 2007 in the Aleutian Islands at a depth of 9 km, recorded at YK. (a) Beams and *F*-traces formed on P′P′ab and P′P′df slownesses and back-azimuths. *F*-vespagrams formed for a range of (b) back-azimuths and (c) slownesses. Predicted times and slownesses from ak135 are shown by green triangles and lines. Observations are marked by blue lines representing onset times and circles showing the maximum *F*-amplitude, accounting for the time separation between the picks and peaks.

P′P′bc and a P′P′ab. Average picking accuracy is ~0.2 s. We calculate P′P′ab-df and P′P′bc-df differential residual times, and P′P′df absolute residual times, where positive and negative residual and absolute times, respectively, indicate a fast inner core; thus, we reverse the sign of P′P′df absolute measurements for comparison with the differential measurements. We apply corrections calculated for the direct *P* wave to account for event mislocation and near-surface structure. For each event, we calculate the signal-to-noise ratio of P′P′df relative to noise in a 10 s long window starting 50 s prior to the predicted arrival of P′P′df.

Differential measurements of P′P′ab-df and P′P′bc-df are used to reduce the influence of unmodeled mantle and source effects. Still, it may be necessary to apply corrections for mantle and crustal structure before attributing the residuals to the inner core (e.g., Bréger et al., 1999). Given the long path of P′P′ab in the lower mantle and its large separation from the P′P′df path, P′P′ab-df residual measurements are less reliable than P′P′bc-df measurements; however, P′P′bc exists only for a small range of source-receiver distances (between major arc distances of 290–311°). At these distances, the direct waves, P′P′ab, P′P′bc, and P′P′df arrive within a short time window, making phase identification difficult. For events at larger source-receiver distances there is greater time separation between phases; thus, we use P′P′df absolute residuals and P′P′ab-df differential residuals to increase our coverage.

3. Results

We observe up to three direct arrivals in the P′P′ time window, and other additional arrivals and noise, discussed in section 4.1. The measured residual arrival times show large scatter but are, on average, low (mean and standard deviation: P′P′ab-df = 1.04 ± 2.72 s, P′P′bc-df = 1.02 ± 2.09 s, and P′P′df = −3.14 ± 2.64 s for data with SNR > 2, Figure 3) compared with up to 10 s predicted by some anisotropy models. These low values are consistent for data with lower signal-to-noise ratios (Figure S7). Residual travel time anomalies show spatial variability. In particular, paths reflecting under the source region of the SSI events show rapid changes in anomalies with small changes in path (Figure 3).

We convert travel time anomalies to velocity anomalies relative to ak135 as $\frac{dT}{T} = \frac{-dV}{V}$, where *T* and *V* are a reference travel time and velocity in the inner core, respectively, to account for differences in inner core path lengths. We attribute the entire travel time anomaly to the inner core. We are unable to separate the influence of the two, differently oriented, paths through the inner core; hence, we consider the residual time as a single cumulative anomaly and characterize the whole P′P′df path by the average of the two angles (ξ_1 and ξ_2) made with the rotation axis. Scatter in the measurements is reduced (mean and standard deviation: P′P′ab-df = 0.49 ± 0.21 s, P′P′bc-df = 0.43 ± 0.26 s, and P′P′df = 0.48 ± 0.26 s for data with SNR > 2, Figure 3). We find a weak trend of increasing velocity anomalies with decreasing average ξ angle (Figure 4), consistent with the results of past P′P′df studies (Bréger, Romanowicz, et al., 2000; Rost & Garnero, 2004).

4. Discussion

Our P′P′df travel time measurements suggest weak anisotropy in the inner core. Here we discuss the reliability of the measurements, possible sources of contamination, the magnitude of the anisotropy relative to previous studies, and the implications for core structure.

4.1. Robustness of Observations

P′P′ is a maximum travel time phase, such that scattering or reflection from dipping reflectors in the crust at locations other than the specular reflection point will produce precursors to the main phase. However, these

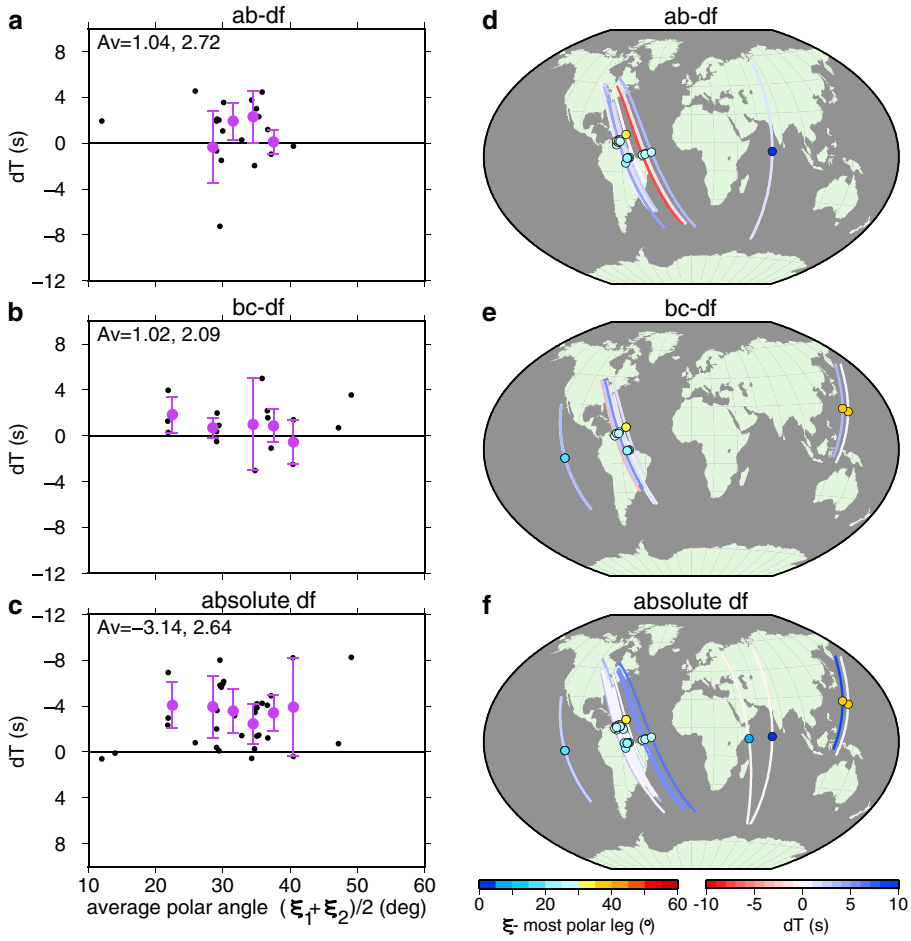

Figure 3. Residual travel times as a function of average angle to the rotation axis for (a) P′P′ab-df and (b) P′P′bc-df differential measurements and (c) P′P′df absolute measurements. Individual measurements are shown by points, while moving averages (in 3° bins with no overlap, for bins containing a minimum of 2 observations) are shown by purple circles with one standard deviation error bars. Residual travel times (line color) plotted along the inner core path, for only the most polar of the source- and receiver-side paths (ξ shown by circle color), for (d) P′P′ab-df differential measurements, (e) P′P′bc-df differential measurements, and (f) P′P′df absolute measurements. Data have SNR $>$ 2; for data at lower SNR values, see Figure S7.

precursory waves arrive from different directions than the main phase (Figure S8). Therefore, we pick waves that arrive with slowness and back-azimuth most consistent with the predictions for the main P′P′ waves. We observe slowness and back-azimuth departures from 1-D model predictions, which, on average, at YK are P′P′df 0.7 s/deg ± 1.0 and 22.5°±15.5, P′P′bc 0.5 s/deg ± 0.2 and 18.2° ± 13.8, and P′P′ab 1.1 s/deg ± 1.2 and 11.4° ± 9.2, and at IL: P′P′df 0.6 s/deg ± 0.5 and 65.3° ± 33.8, P′P′bc 0.4 s/deg ± 0.3 and 38.9° ± 26.1, and P′P′ab 1.5 s/deg ± 1.0 and 57.8° ± 40.4. Furthermore, we find that the slowness of P′P′ab is more sensitive to small changes in lower mantle velocities than P′P′df or P′P′bc.

We perform resolution tests to determine the ability of the arrays to correctly determine slowness and back-azimuth for P′P′. We use a synthetic wavelet of a similar duration to our data, combined with real noise from each array, scaled to have SNR of 2, and filter the data between 0.4 and 1.5 Hz. We find that back-azimuth resolution strongly depends upon incoming slowness (Table S2). For slownesses typical of P′P′df (~0.5 to 1.5 s/deg), we expect to resolve the signal to within, on average, 1.0 s/deg slowness and ~65° back-azimuth for IL, and 0.2 s/deg slowness and 10° back-azimuth for YK. Thus, especially for the lower slowness signals at IL, large azimuthal anomalies are expected. Disparities in resolution limits between the arrays result from differences in the width (aperture) of the array and the distribution of stations.

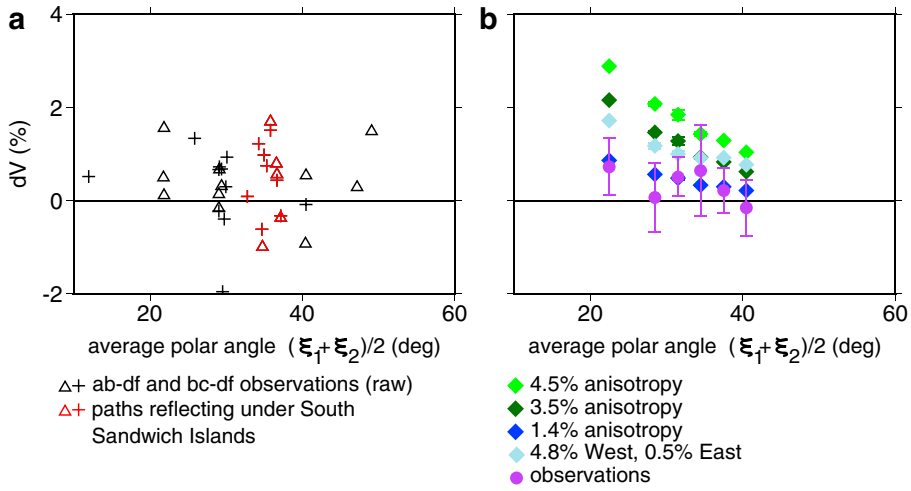

Figure 4. Observed velocity anomalies from P′P′ab-df and P′P′bc-df differential residual travel times, as a function of average angle to the rotation axis. (a) Raw measurements for all observations displayed as crosses and triangles for P′P′ab-df and P′P′bc-df, respectively (SNR > 2). Velocity anomalies for paths reflecting under the South Sandwich Islands source region are shown in red. (b) Moving averages (calculated as in Figure 3) of observed velocity anomalies (purple circles) with one standard deviation error bars and predicted velocity anomalies calculated from several anisotropy models for the observed events (diamonds).

4.2. Possible Contamination by Mantle Structure

The variability in travel time residuals may result from heterogeneity on other parts of the path. While differential measurements and *P* wave corrections should account for crust and upper mantle structure and source mislocations, the influence of lower mantle structure may remain. In addition, strong anomalies resulting from subducted slabs could cause significant travel time anomalies between the two paths in a differential phase pair (Helffrich & Sacks, 1994; Weber, 1990). Laterally varying upper mantle structure could contribute to the scatter that we observe here, but it is unlikely to be the sole cause of the positive velocity anomaly.

To evaluate the influence of not-accounted-for mantle structure, we calculate corrections for the P′P′ phases from several global tomographic models by 1D ray tracing through the model and calculating the anomaly accumulated along the path. We use *P* wave models GAP_P4 (Obayashi et al., 2013) and MIT_P08 (Li et al., 2008) and *S* wave models S40RTS (Ritsema et al., 2011) and SEMUCB-WM1 (French & Romanowicz, 2014). The *S* wave models are scaled to *P* wave velocities using a constant factor of 0.5 for SEMUCB-WM1 and, for S40RTS, a factor linearly decreasing from 0.8 at the surface to 0.33 at the CMB (Ritsema and van Heijst, 2002). Differential mantle corrections are, on average, small at around 0.2 s for P′P′ab-df and P′P′bc-df and 0.3 to 0.7 s for P′P′df. Nonetheless, the corrections often reduce the spread of outliers implying that some of the scatter does result from mantle structure (Figures S9 and S10). However, tomographic methods only resolve the broader scales of mantle heterogeneity (100 s to 1,000 s km); thus, the true corrections for mantle structure may be larger.

Strongly anomalous and laterally discontinuous, small-scale lower mantle structures, such as ultra-low velocity zones (ULVZs) and the D″ layer, may cause sharp changes in differential travel times between closely located paths (Bréger, Tkalcic, et al., 2000), potentially influencing one phase of a P′P′ pair while leaving the travel time of the other unperturbed. To generate the observed positive residual times a ULVZ would have to delay the P′P′ab or P′P′bc phase or the region outside of the ULVZ would need to advance the P′P′df wave. For parameters typical of ULVZs (Garnero & Helmberger, 1998; Rost et al., 2006) and fast regions in D″ (Weber & Körnig, 1992), even for the longest possible P′P′ab and P′P′df paths with the greatest possible separation and the most time spent in the lower mantle, these structures would produce travel time anomalies of around 1.5 s and 0.6 s, respectively. Multiple interactions with ULVZs or fast regions of D″ could produce significant travel time anomalies, but this is unlikely. Thus, while localized mantle structure may explain some of the observed scatter, it would be insufficient to explain all of the differential travel time residuals.

Topography on either the CMB or inner core boundary (ICB) could cause differential travel-time anomalies, depending on ray piercing location. Scales of CMB topography are not well known but are estimated to be less than 2 km in height (e.g., Soldati et al., 2012) that would produce a maximum of 0.01 s for P′P′ab-df and less so for P′P′bc-df. Meanwhile, the maximum estimate ICB topography of 5 km amplitude over 10 km vertical scale (Cao et al., 2007) would produce a 0.04 s anomaly. While four boundary crossings of P′P′ would multiply these anomalies, the total would still be below the pick resolution, thus likely undetectable.

4.3. Strength of Anisotropy

We compare the inferred P′P′ anisotropy to several inner core anisotropy models constructed from PKP (Irving & Deuss, 2011). Using the PKP models, we predict the overall velocity anomaly each P′P′ path would experience by combining the velocity anomaly along each inner core leg according to its ξ angle. We make predictions for uniform anisotropy models and hemispherical anisotropy models where each P′ leg experiences one of two anisotropic structures depending on the location of the P′ path midpoint, according to hemisphere boundaries derived from Irving and Deuss (2011). The hemispherical PKP model is less anisotropic in the eastern (0.5%) than in the western (4.8%) hemisphere. While previous studies have found hemispherical isotropic velocity anomalies in the upper inner core (Waszek et al., 2011), with the exception of two paths, our P′P′ data sample both fast and slow isotropic hemispheres; thus, the effect of this layer would cancel out.

We find large scatter in the absolute P′P′df residuals; thus, we compare data with and without them to the PKP anisotropy models. Without the P′P′df data our observations most closely match predictions from the uniform model with 1.4% anisotropy, which is much weaker than most PKPdf models (Figure 4). An exception to this is the small range of ξ angles dominated by paths reflecting under the SSI, where observed velocity anomalies are, on average, larger than those at both greater and smaller ξ angles. When events reflecting under the SSI are removed, the remaining observations even better match the 1.4% anisotropy model (Figure S11). When the P′P′df data are included and a moving average is calculated to reduce the influence of outliers, our data show slightly stronger anisotropy of 1.5–2% (Figure S12). Both with and without P′P′df data, our observations are significantly weaker than the PKP model constructed using both eastern and western hemisphere anisotropy models from Irving and Deuss (2011).

The P′P′ differential travel times represent the cumulative effect of inner core structure; thus, we are unable to determine where along either of the two inner core paths the travel time anomaly is acquired. We construct a range of synthetic inner core anisotropy models by scaling an existing one. We grid search for the strength of anisotropy on the east and west hemispheres that minimizes the RMS misfit between the synthetic velocity anomaly (of both hemispheres combined) and the observed velocity anomaly for all data at all ξ angles (Figure S13). The best fitting anisotropy strongly depends on the data used and minima are poorly constrained. When absolute P′P′df observations are included, the data are best fit by a model with ~1% anisotropy in the western hemisphere and close to no anisotropy in the eastern hemisphere. Meanwhile, when only P′P′ab-df and P′P′bc-df observations are used, the data are best fit by either 1% anisotropy in the eastern hemisphere and no anisotropy in the western hemisphere, or roughly uniform anisotropy of ~0.5%. When data from paths reflecting under the South Sandwich Islands are included, the best fitting model shows stronger anisotropy in the western hemisphere. While this suggests some interesting trends, we are reluctant to interpret them given the nonunique results.

4.4. Testing of Model Robustness

We construct a new model of cylindrical inner core anisotropy as a perturbation to a spherically symmetric model, parameterized as (Creager, 1992)

$$\frac{\delta v}{v} = a + b\cos^2\xi + c\ \cos^4\xi \tag{2}$$

where v and δv represent the reference velocity and velocity perturbations, respectively. Coefficient a represents the difference between the apparent equatorial velocity and the reference model, b and c describe the variation of anisotropic velocity as a function of ξ, and the maximum amplitude of the anisotropy is thus $b+c$. We fit a curve to the data using an L1-norm to account for outliers. As we have no constraints beyond $\xi = 50°$, the model is required to reach 0% anisotropy at $\xi = 90°$.

We test the robustness of this model by bootstrapping the data set. We calculate the mean and standard deviation across 1,000 bootstrapped models and derive coefficients a, b, and c for this model. We construct one isotropic model ($b = c = 0$) to test the misfit reduction. Applying mantle corrections to the residual times and recalculating the anisotropy model results in negligible improvements of the fit for all tomographic models (Figure S14). Coefficients and RMS misfit for all models are given in Table S3. We find anisotropy of ~0.5%, weaker than observed in the moving averages (Figure 4b), as the curve tries to account for the observation of a lower velocity anomaly (0.4%) closer to the rotation axis (~15°) rather than anomalies further away from it. The standard deviation of the bootstrapped models, which includes models where this data point has been removed, ranges from 0 to 1% anisotropy.

4.5. Implications for Core Structure

Paths reflecting under the SSI show larger velocity anomalies and greater scatter than other paths at lower ξ. This supports previous observations of variability in PKPdf velocity anomalies on similar paths (Romanowicz et al., 2003; Romanowicz & Wenk, 2017; Tkalcic, 2010). The cause of this variability may be in the inner or outer cores, or within the mantle. Possibly, the structure of the subducting slab in the South Sandwich Islands may influence differential travel times and might not be suitably represented in global tomographic models.

The anisotropic velocity structure of the inner core relates to its composition, physical state, and dynamics. Experiments and first-principles calculations show uncertainty over whether the inner core comprises hexagonally close-packed (hcp) or body-centered cubic (bcc) iron (Belonoshko et al., 2008; Mikhaylushkin et al., 2007; Modak et al., 2007; Tateno et al., 2010). While the anisotropy of a single crystal depends on its phase, the effective anisotropy of the bulk core will also depend on the degree of alignment of the crystals. Dynamic models of core growth have suggested that cubic phases of iron (bcc and face-centered cubic) could produce global anisotropy up to 1% seismic anisotropy but more likely ~0.5% (Lincot et al., 2015), while hcp iron could produce 1–3% anisotropy (Lincot et al., 2016), depending on the dominant slip system of plastic deformation and method of core growth. Other methods suggest that global anisotropy would be similar for a core comprising hcp or a bcc fiber structure (Romanowicz et al., 2015). Our observations imply that either crystal structure is possible, but that the inner core may not need to be as strongly anisotropic as previously thought. The lateral variability in observed travel times suggests either an inner core comprising multiple domains (Tkalcic, 2010), potentially generated by variability in the degree of crystal alignment (Lincot et al., 2015), or heterogeneity within or outside of the inner core.

5. Conclusion

We have assembled a data set of travel time anomalies for P′P′ waves traveling through the inner core at previously unsampled locations. Our observations indicate at most 0.5–1.5% anisotropy aligned with the Earth's rotation axis, confirming the results of Bréger, Romanowicz, et al. (2000) and Rost and Garnero (2004). Anisotropy in the inner core may not be as strong as suggested in some recent studies. However, for paths with P′P′ surface reflections located near the SSI, residual travel times show large variability, consistent with PKPdf observations. This suggests anomalous local structure within the inner core, in the upper mantle, under the SSI, or any part of the mantle and core sampled by these paths.

Acknowledgments
We thank the Prototype International Data Centre (pIDC) for development and distribution of the REB and the CTBTO for access to the waveform data from the IMS arrays. Waveform data for the Yellowknife and Eilson arrays are available from the Canadian National Data Centre at http://www.earthquakescanada.nrcan.gc.ca/stndon/AutoDRM/autodrm_req-en.phpcndc and the Incorporated Research Institutions for Seismology at http://ds.iris.edu/ds/nodes/dmc/forms/breqfast-request/, respectively. Our measurements are presented in Table S4. This work was supported by NSF grants EAR-1135452 and EAR-1417229.

References

Beghein, C., & Trampert, J. (2003). Robust normal mode constraints on inner-core anisotropy from model space search. *Science*, *299*(5606), 552–555. https://doi.org/10.1126/science.1078159

Belonoshko, A., Skorodumova, N. V., Rosengren, A., & Johansson, B. (2008). Elastic anisotropy of Earth's inner core. *Science*, *319*(5864), 797–800. https://doi.org/10.1126/science.1150302

Blandford, R. R. (1974). An automatic event detector at the Tonto Forest seismic observatory. *Geophysics*, *39*(5), 633–643. https://doi.org/10.1190/1.1440453

Bréger, L., Romanowicz, B., & Tkalcic, H. (1999). PKP(BC-DF) travel time residuals and short scale heterogeneity in the deep Earth. *Geophysical Research Letters*, *26*, 3169–3172. https://doi.org/10.1029/1999GL008374

Bréger, L., Romanowicz, B. A., & Rousset, S. (2000). New constraints on the structure of the inner core from P′P′. *Geophysical Journal International*, *27*(17), 2781–2784.

Bréger, L., Tkalcic, H., & Romanowicz, B. A. (2000). The effect of D on PKP (AB-DF) travel time residuals and possible implications for inner core structure. *Earth and Planetary Science Letters*, *175*(1-2), 133–143. https://doi.org/10.1016/S0012-821X(99)00286-1

Cao, A., Masson, Y., & Romanowicz, B. (2007). Short wavelength topography on the inner-core boundary. *Proceedings of the National Academy of Sciences of the United States of America*, *104*(1), 31–35. https://doi.org/10.1073/pnas.0609810104

Cao, A., & Romanowicz, B. (2007). Test of the innermost inner core models using broadband PKIKP travel time residuals. *Geophysical Research Letters*, *34*, L08303. https://doi.org/10.1029/2007GL029384

Creager, K. C. (1992). Anisotropy of the inner core from differential travel times of the phases PKP and PKIKP. *Nature*, *356*(6367), 309–314. https://doi.org/10.1038/356309a0

Davies, D., Kelly, E. J., & Filson, J. R. (1971). Vespa process for analysis of seismic signals. *Nature Physical Science*, *232*(27), 8–13. https://doi.org/10.1038/physci232008a0

Deuss, A. F. (2014). Heterogeneity and anisotropy of Earth's inner core. *Annual Review of Earth and Planetary Sciences*, *42*(1), 103–126. https://doi.org/10.1146/annurev-earth-060313-054658

French, S. W., & Romanowicz, B. A. (2014). Whole-mantle radially anisotropic shear velocity structure from spectral-element waveform tomography. *Geophysical Journal International*, *199*(3), 1303–1327. https://doi.org/10.1093/gji/ggu334

Garnero, E. J., & Helmberger, D. V. (1998). Further structural constraints and uncertainties of a thin laterally varying ultralow-velocity layer at the base of the mantle. *Journal of Geophysical Research*, *103*, 12,495–12,509. https://doi.org/10.1029/98JB00700

Helffrich, G., & Sacks, S. (1994). Scatter and bias in differential PKP travel times and implications for mantle and core phenomena. *Geophysical Research Letters*, *21*, 2167–2170. https://doi.org/10.1029/94GL01876

International Seismological Centre (2014). On-line bulletin, Internatl. Seismol. Cent., Thatcham, United Kingdom. Retrieved from http://www.isc.ac.uk

Irving, J. C. E. (2016). Imaging the inner core under Africa and Europe. *Physics of the Earth and Planetary Interiors*, *254*, 12–24. https://doi.org/10.1016/j.pepi.2016.03.001

Irving, J. C. E., & Deuss, A. (2011). Hemispherical structure in inner core velocity anisotropy. *Journal of Geophysical Research*, *116*, B04307. https://doi.org/10.1029/2010JB007942

Ishii, M., & Dziewonski, A. M. (2002). The innermost inner core of the Earth: Evidence for a change in anisotropic behavior at the radius of about 300 km. *Proceedings of the National Academy of Sciences of the United States of America*, *99*(22), 14,026–14,030. https://doi.org/10.1073/pnas.172508499

Kennett, B. L. N., Engdah, E. R., & Buland, R. (1995). Constraints on seismic velocities in the Earth from traveltimes. *Geophysical Journal International*, *122*(1), 108–124. https://doi.org/10.1111/j.1365-246X.1995.tb03540.x

Kennett, B. L. N., & Gudmundsson, O. (1996). Ellipticity corrections for seismic phases ellipticity corrections for seismic phases. *Geophysical Journal International*, *127*(1), 40–48. https://doi.org/10.1111/j.1365-246X.1996.tb01533.x

Li, C., van der Hilst, R. D., Engdahl, E. R., & Burdick, S. (2008). A new global model for P wave speed variations in Earth's mantle. *Geochemistry, Geophysics, Geosystems*, *9*, Q05018. https://doi.org/10.1029/2007GC001806

Li, X. & Cormier, V. F. (2002). Frequency-dependent seismic attenuation in the inner core 1. A viscoelastic interpretation. *Journal of Geophysical Research*, *107*(B12), 2361.

Lincot, A., Cardin, P., Deguen, R., & Merkel, S. (2016). Multiscale model of global inner-core anisotropy induced by hcp-alloy plasticity. *Geophysical Research Letters*, *43*, 1084–1091.

Lincot, A., Merkel, S., & Cardin, P. (2015). Is inner core seismic anisotropy a marker for plastic flow of cubic iron? *Geophysical Research Letters*, *42*, 1326–1333. https://doi.org/10.1002/2014GL062862

Lythgoe, K. H., Deuss, A. F., Rudge, J. F., & Neufeld, J. A. (2014). Earths inner core: Innermost inner core or hemispherical variations? *Earth and Planetary Science Letters*, *385*, 181–189. https://doi.org/10.1016/j.epsl.2013.10.049

Mikhaylushkin, A. S., Simak, S. I., Dubrovinsky, L., Dubrovinskaia, N., Johansson, B., & Abrikosov, I. A. (2007). Pure iron compressed and heated to extreme conditions. *Physical Review Letters*, *99*, 1–4.

Modak, P., Verma, A. K., Rao, R. S., Godwal, B. K., Stixrude, L., & Jeanloz, R. (2007). Stability of the hcp phase and temperature variation of the axial ratio of iron near Earth-core conditions. *Journal of Physics: Condensed Matter*, *19*, 1–9.

Monnereau, M., Calvet, M., Margerin, L., & Souriau, A. (2010). Lopsided growth of Earth's inner core. *Science*, *328*(5981), 1014–1017. https://doi.org/10.1126/science.1186212

Morelli, A., Dziewonski, A. M., & Woodhouse, J. H. (1986). Anisotropy of the inner core inferred from PKIKP travel times. *Geophysical Research Letters*, *13*, 1545–1548. https://doi.org/10.1029/GL013i013p01545

Nguyen, J. H., & Holmes, N. C. (2004). Melting of iron at the physical conditions of the Earth's core. *Nature*, *720*, 339–342.

Obayashi, M., Yoshimitsu, J., Nolet, G., Fukao, Y., Shiobara, H., Sugioka, H., … Gao, Y. (2013). Finite frequency whole mantle P wave tomography: Improvement of subducted slab images. *Geophysical Research Letters*, *40*, 5652–5657. https://doi.org/10.1002/2013GL057401

Ritsema, J., Deuss, A. F., van Heijst, H. J., & Woodhouse, J. H. (2011). S40RTS: A degree-40 shear-velocity model for the mantle from new Rayleigh wave dispersion, teleseismic traveltime and normal-mode splitting function measurements. *Geophysical Journal International*, *184*(3), 1223–1236. https://doi.org/10.1111/j.1365-246X.2010.04884.x

Ritsema, J., & van Heijst, H. J. (2002). Constraints on the correlation of P - and S -wave velocity heterogeneity in the mantle from P, PP, PPP and PKP ab traveltimes. *Geophysical Journal International*, *149*, 482–489.

Romanowicz, B., Tkalcic, H., & Breger, L. (2003). On the origin of complexity in PKP travel time data. In V. Dehant, et al. (Eds.), *Earth's Core: Dynamics, structure, rotation, geodynamics series 31* (pp. 31–44). Washington, DC: American Geophysical Union.

Romanowicz, B., Cao, A., Godwal, B., Wenk, R., Ventosa, S., & Jeanloz, R. (2015). Seismic anisotropy in the Earth's innermost inner core : testing structural models against mineral physics predictions. *Geophysical Research Letters*, *43*, 93–100. https://doi.org/10.1002/2015GL066734

Romanowicz, B., & Wenk, H.-R. (2017). Anisotropy in the deep Earth. *Physics of the Earth and Planetary Interiors*, *269*, 58–90.

Rost, S., & Garnero, E. J. (2004). A study of the uppermost inner core from PKKP and PP differential traveltimes. *Geophysical Journal International*, *156*(3), 565–574. https://doi.org/10.1111/j.1365-246X.2004.02139.x

Rost, S., Garnero, E. J., & Williams, Q. (2006). Fine-scale ultralow-velocity zone structure from high-frequency seismic array data. *Journal of Geophysical Research*, *111*, B09310. https://doi.org/10.1029/2005JB004088

Selby, N. D. (2008). Application of a generalized F detector at a seismometer array. *Bulletin of the Seismological Society of America*, *98*(5), 2469–2481. https://doi.org/10.1785/0120070282

Soldati, G., Boschi, L., & Forte, A. M. (2012). Tomography of core-mantle boundary and lowermost mantle coupled by geodynamics. *Geophysical Journal International*, *189*, 730–746. https://doi.org/10.1111/j.1365-246X.2012.05413.x

Sun, X., & Song, X. (2008). The inner core of the Earth: Texturing of iron crystals from three-dimensional seismic anisotropy. *Earth and Planetary Science Letters*, *269*(1-2), 56–65. https://doi.org/10.1016/j.epsl.2008.01.049

Tanaka, S., & Hamaguchi, H. (1997). Degree one heterogeneity and hemispherical variation of anisotropy in the inner core from PKP(BC)-PKP(DF) times. *Journal of Geophysical Research*, *102*, 2925–2938. https://doi.org/10.1029/96JB03187

Tateno, S., Hirose, K., Ohishi, Y., & Tatsumi, Y. (2010). The structure of iron in the Earth's inner core. *Science*, *330*(6002), 359–361. https://doi.org/10.1126/science.1194662

Tkalcic, H. (2010). Large variations in travel times of mantle sensitive seismic waves from the South Sandwich Islands: Is the Earth's inner core a conglomerate of anisotropic domains? *Geophysical Research Letters*, *37*, L14312. https://doi.org/10.1029/2010GL043841

Tkalcic, H. (2015). Complex inner core of the Earth: The last frontier of global seismology. *Reviews of Geophysics*, *53*, 59–94. https://doi.org/10.1002/2014RG000469

Wang, T., Song, X., & Xia, H. (2015). Equatorial anisotropy in the inner part of Earth's inner core from autocorrelation of earthquake coda. *Nature Geoscience*, *8*, 1–4. https://doi.org/10.1038/NGEO2354

Waszek, L., Irving, J., & Deuss, A. (2011). Reconciling the hemispherical structure of Earth's inner core with its super-rotation. *Nature Geoscience*, *4*(4), 264–267. https://doi.org/10.1038/ngeo1083

Weber, M. (1990). Subduction zones—Their influence on travel times and amplitudes of P-waves. *Geophysical Journal International*, *101*(3), 529–544. https://doi.org/10.1111/j.1365-246X.1990.tb05568.x

Weber, M., & Körnig, M. (1992). A search for anomalies in the lowermost mantle using seismic bulletins. *Physics of the Earth and Planetary Interiors*, *73*(1-2), 1–28. https://doi.org/10.1016/0031-9201(92)90104-4

Wenk, H.-R., Baumgardner, J. R., Lebensohn, R. A., & Tome, C. N. (2000). A convection model to explain anisotropy of the inner core. *Journal of Geophysical Research*, *105*, 5663–5677.

Woodhouse, J. H., Giardini, D., & Li, X.-D. (1986). Evidence for inner core anisotropy from free oscillations. *Geophysical Research Letters*, *13*, 1549–1552.